

YUKI algorithm and POD-RBF for Elastostatic and dynamic crack identification

Brahim Benaissa¹, Nourredine Aït Hocine², Samir Khatir³⁻⁴, Mohamed Kamel Riahi⁵⁻⁶, Seyedali Mirjalili⁷⁻⁸.

¹Toyota Technological Institute, Department of Mechanical Systems Engineering, Design Engineering Lab, 468-8511 Aichi, Nagoya, Tempaku Ward, Hisakata, 2 Chome-12-1, Japan

²INSA CVL, Univ. Tours, Univ. Orléans, LaMé, 3 rue de la Chocolaterie, CS 23410, 41034, Blois, Cedex, France

³Soete Laboratory, Faculty of Engineering and Architecture, Ghent University, Technologiepark Zwijnaarde 903, B-9052, Zwijnaarde, Belgium

⁴Faculty of Civil Engineering, Ho Chi Minh City Open University, Ho Chi Minh City, Viet Nam.

⁵Department of Mathematics, Khalifa University of Sciences and Technology, P.O. Box 127788, Abu Dhabi, United Arab Emirates.

⁶Emirates Nuclear Technology Center (ENTC), Khalifa University of Science and Technology, United Arab Emirates

⁷Centre for Artificial Intelligence Research and Optimisation, Torrens University Australia, Fortitude Valley, Brisbane, 4006, QLD, Australia

⁸Yonsei Frontier Lab, Yonsei University, Seoul, Korea

Abstract. This paper proposes a new metaheuristic algorithm with a search space reduction capability guided by simple formalism. The search population focuses partially on the inside the local search area while the rest explore globally, looking for better search areas. We call the new algorithm by YUKI (YA) and employ it in a crack identification problem. With the aid of a set of measurements taken on the defected structure, we aim at identifying the crack parameters such as length and orientation. To this end, we use the so-called model reduction technique through Proper orthogonal Decomposition (POD) endorsed with Radial Basic Function (RBF), which helps in predicting (numerically) the measurement at new points (out of the set of sensors) via interpolation. This method is widely used in this context and was proven very effective computational-wise. In our study of the performance of YA, we deal with two cases; Firstly, in the case of the Elastostatic study. And secondly, in the case of dynamic analysis. We compare the performance of the suggested algorithm with the performance of well-known optimization methods, such as Teaching Learning Based Optimization (TLBO), Cuckoo Search (CS), and the Grey Wolf Optimizer (GWO). The results show that YA provides accurate and faster results compared to the mentioned algorithms.

Keywords: YA, POD-RBF, Crack identification, Inverse problem, Static and Dynamic Analysis.

1 Introduction

Structural health monitoring (SHM) is essential for engineering applications such as beams, plates, bridges, and offshore. Inverse crack identification predicts the unknown crack characteristics inside a structure (size, position, and orientation) using the structural response to an exerted excitation. Theoretical backgrounds related to inverse crack identification in mechanics are thoroughly developed; we refer the reader to [1-3]. Elastostatic approaches consider crack identification as a geometrical inverse problem based on measurable data for given boundary conditions, namely the material properties, geometry, and loading conditions [3, 4]. On the other hand, approaches based on dynamic studies formulate the problem using the vibrational response of structures [5, 6]. There exist non-mechanical crack detection techniques such as [7-9].

In inverse crack identification, the evaluation function generally compares, in an iterative search, between the measured structural response and the estimated counterpart. In such cases, where the behavior is not linear, metaheuristic optimization methods are powerful tools for predicting the unknown crack parameters by minimizing such comparison function at the cost of significant computational efforts. Moreover, they often require thousands of fitness evaluations, corresponding to several simulation runs at every iteration [4, 10-19]. Nonetheless, model reduction techniques contribute heavily to such computationally demanding approaches.

Proper Orthogonal Decomposition (POD) is an efficient model reduction technique based on the projection of the original model onto a subspace using full model snapshots [20-22]. This method offers a computational cost advantage [23-27]. Winton et al. [23], the authors coupled the POD with Levenberg–Marquardt optimization to approximate the property of hydraulic conductivity in saturated domains. Furthermore, in [24], this model reduction method has been used to estimate unknown heat conductivities and film coefficient distribution. Brigham et al. [25] presented a POD and Finite Element Method for Isocoelastic material characterization. Finally, Rogers et al. [26] tackled the conduction problem in different structures to estimate the Isotropic material parameters of a 3D bar in tension.

Radial Basis Functions (RBF) is a powerful interpolation method characterized by handling a random distribution of data points. It gives the possibility to consider a large number of variables [28-35]. In [28], Buljak and Mier developed the POD-RBF approach based on simulation data to estimate material properties in the indentation test. Similarly, in [29], Hoang et al. used this method to characterize interface tissue in dental implant systems. In [32], POD-RBF is used to estimate the depth residual stress profiles induced by surface treatment of metal components. Also allowed using data that is entirely experimental [36]. In [22] POD-RBF model is built up based on the vibration response of a composite beam to identify crack position and size. In [37], Bocciarelli et al. used the POD-RBF techniques to characterize metallic materials in the case indentation test using experimental data. Deep Neural Networks (DNN) are being used to advance damage identification research. In [38], Cosmin et al. suggest an approach to the boundary values problem. The mesh-free method uses scattered sets of points in the training and evaluation sets. Such learning methods can be used for solving the forward and inverse problem simultaneously.

Metaheuristic techniques have become popular over the last decade. The popularity of these algorithms is due to several factors, including their versatility, gradient-free mechanism, and avoidance of local optima. The first two benefits stem from the fact that metaheuristics only look at the inputs and outputs when considering and solving optimization problems. They are highly adaptable when it comes to solving ill-posed inverse problems. Artificial bee colony algorithm was used in flaws prediction

problem, using extended Finite Element Method (XFEM) in a dynamic study of a plate [5]. Genetic Algorithm (GA) was used in [6, 39] to detect cracks in flat membrane structures under static and dynamic loads. [40] compares the performance of Particle Swarm Optimization to GA in the crack identification study based on POD-RBF. Jaya algorithm is used with Artificial Neural Network to identify crack size and orientation based on experimental vibration modes [41].

This paper suggests a new metaheuristic algorithm to solve the inverse crack identification problem. We are considering two cases. The first case is an Elastostatic study based on FEM. And the second is the dynamic study based on experimental data. Furthermore, finally, we compare the performance of the suggested algorithm to the well-known algorithms. Namely Cuckoo Search (CS) [42], Teaching Learning Based Optimization (TLBO) [43], and the Grey Wolf Optimizer (GWO) [44].

We organize the rest of the paper as follows: Section 2 describes the YUKI algorithm in detail. In Section 3, we present the POD-RBF method. Section 4 discusses the crack identification formulation in the Elastostatic study, where first, we present the POD-RBF model details and the prediction validation with FEM results. Sections 4.3 to 4.5 discuss the crack identification results in cases of different crack sizes and orientations, with noisy data, and with a limited number of sensors. Section 4.6 compares the performance of YA to other algorithms in terms of precision and computational cost. Section 5 discusses crack identification in the case of a dynamic study based on experimental data. In 5.1, we present the experimental setup. In section 5.2, the POD-RBF model details are presented, followed by validation with experimental output. Finally, in Sections 5.3 and 5.4, the results of crack identification are discussed, Comparing YA with other algorithms in terms of precision and computational cost.

2 Yuki algorithm for inverse crack identification

This algorithm suggests a principle of dynamic search space reduction. By creating a local search area around the absolute best solution found so far. The algorithm adapts the size of the search area dynamically throughout the progress of the search, using the distance between two points as a reference.

The first point is the absolute best point. It corresponds to the minimum fitness value. Furthermore, The second point is called MeanBest. We calculate this point as the center of the “best points” cloud. The best points here are the best solutions found so far by each member of the YA population.

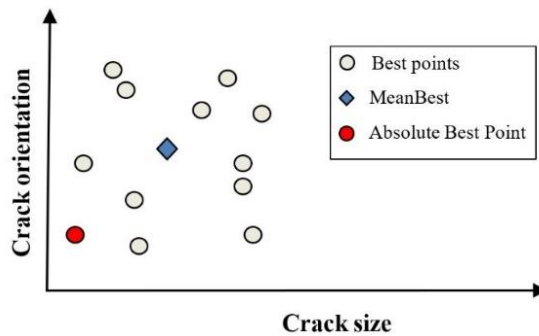


Figure 1. Illustration of the MeanBest point.

The following expression calculates the local boundaries:

$$D = |X_{best} - X_{MeanBest}| \quad (1)$$

$$LT = X_{best} + D \quad (2)$$

$$LB = X_{best} - D \quad (3)$$

Respectively LT and LB are the Local top and bottom boundaries of the local search space. Furthermore X_{best} Is the point corresponding to the absolute best fitness value at the current iteration. And the term $X_{MeanBest}$ is the mean of the Best Points vector.

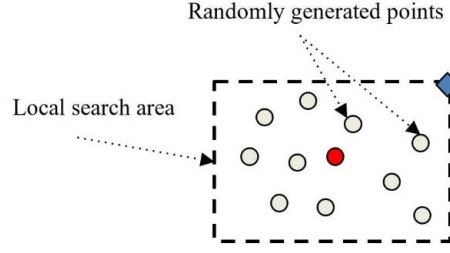


Figure 2. Illustration of the local search area. The red circle stands for the absolute best point, and the blue rhombus represents the MeanBest point.

The second concept is to create a random distribution of points X_{loc} Inside the local search area, split the search into two parts; One part of the population to explore outside the local search area. The other is assigned to focus on searching around the center of the search area. The size of the exploration population changes iteratively in this manner:

$$if \text{rand} < 1 - K / K_{max} \quad (4)$$

Eq. 4 condition compares the randomly generated value, between 0 and 1, to the output of the Eq. 4 expression, which is also between 0 and 1. K is the current iteration and K_{max} Represent the value of maximum iteration set initially as a stopping criterion. At early iterations, the output corresponds to a high possibility for the “if statement” to be True, and at late iterations, this possibility decreases linearly. This way, we assign most of the population toward exploring initially, then slowly shift toward exploitation.

Exploration population look in the direction away from the MeanBest expressed as follows:

$$E = X_{loc} - \text{randi}(10) \times X_{MeanBest} \quad (5)$$

Where $\text{randi}(4)$ is a random integer between 1 and the value of the exploration control parameter chosen as an integer between 2 and 10, the following equation calculates the new solutions:

$$X_{new} = X_{loc} + \text{rand} \times E \quad (6)$$

“rand” here stands for a random value between 0 and 1. Note here that we use the same random value for all design variables.

The rest of the population, not assigned to exploration, is pushed to search around the local area center. The following equation governs this process:

$$F = X_{loc} - X_{best} \quad (7)$$

$$X_{new} = X_{loc} - \text{rand} \times F \quad (8)$$

Where F is the distance between the selected local point to the absolute best solution, similarly, rand here is the random value between 0 and 1. Note also here that we use the same random value for all design variables.

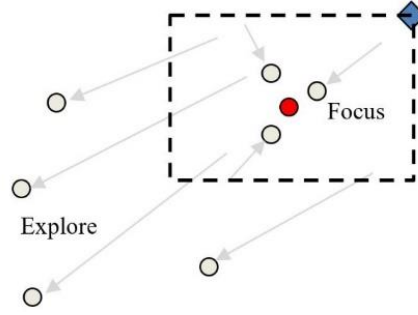


Figure 3. Illustration of the exploration and focus concepts.

We update the absolute best solution and the individual best solutions at the end of each iteration. For details, Fig.4 shows the YA pseudo-code.

In this study of crack identification, the fitness function is:

$$\begin{cases} f(\mathbf{P}) = \frac{\|\mathbf{u}(\mathbf{P}_0) - \mathbf{u}(\mathbf{P})\|^2}{\|\mathbf{u}(\mathbf{P}_0)\|^2} \\ f(\mathbf{P}_{optimal}) = \min [f(\mathbf{P})] \end{cases} \quad (9)$$

Where the response vectors $\mathbf{u}(\mathbf{P})$ of the suggested cracks is compared to the reference response $\mathbf{u}(\mathbf{P}_0)$ That was caused by the unknown crack.

The following points discuss the theory of the suggested algorithm.

- By exporting new areas situated away from the MeanBest point, we focus the exploration effort in one direction, which increases the possibility of finding new solutions compared to randomly exploring the global area.
- By multiplying the MeanBest value to a random integer, we create a pulsating effect, essential for suggesting different solutions in every iteration. It also helps extend the reach of the search.
- As long as there is good coverage of the global search space, the distance between Best Points remains safely large. Thus the local search area avoids collapsing on a local optimum.
- The search area sizes are independent across search dimensions. Because this algorithm can create variations for which the local search area is significant in one dimension and very small in another dimension. Thus the search focus is reacting to the sensitivity of each design variable.
- The local search area's size can increase dynamically if the algorithm finds a new best solution far from the current local search area.
- As solutions converge to the optimum, the local search area gets smaller,

Yuki algorithm pseudo-code

Load the search parameters
Initiate the population X
Evaluate the fitness
Calculate the $X_{MeanBest}$ and X_{best}
for $K = 1$ to K_{max}
 Calculate the local boundaries
 Generate the local population randomly
 if $rand < 1 - K / K_{max}$
 Calculate the exploration solutions
 else
 Calculate focus solutions
 end
 update the $X_{MeanBest}$
 update the X_{best} if better solutions are found
end
return X_{best}

Figure 4. YUKI Algorithm.

3 POD-RBF for static crack identification problem

POD is used in this study, coupled with the interpolation method RBF to provide the structural response in the inverse problem. Based on data measured a priori and stored in the matrix \mathbf{U} .

$$\mathbf{U} = \begin{bmatrix} u_1^1 & u_1^2 & \cdots & u_1^S \\ u_2^1 & u_2^2 & \cdots & u_2^S \\ \vdots & \vdots & \ddots & \vdots \\ u_N^1 & u_N^2 & \cdots & u_N^S \end{bmatrix} \quad (10)$$

\mathbf{U} is constituted of N snapshots, denoted as u^j (for $j = 1, 2 \dots S$). S is the size of the snapshot vector. In this study, the size of the structural response data. On the other hand, the matrix $\mathbf{P} = ([\mathbf{L}_1, \boldsymbol{\theta}_1], \dots, [\mathbf{L}_N, \boldsymbol{\theta}_N])$ stores the crack parameters. \mathbf{L} is the crack length, and $\boldsymbol{\theta}$ is its orientation. In the Elastostatic study, detailed in section 4.1, the snapshot consists of boundary displacement measurements at boundary nodes. Furthermore, in the dynamic study, detailed in section 5.2, the Frequency Response Function measurements constitute the snapshot matrix.

At this point, we extract a set of orthogonal vectors $\boldsymbol{\Phi}$, upon which we project the measurement data matrix \mathbf{U} to obtain the amplitude matrix \mathbf{A} as follows:

$$\mathbf{A} = \boldsymbol{\Phi}^T \cdot \mathbf{U} \quad (11)$$

Matrix \mathbf{A} approximates the structural response data. It is worth noticing here that we calculate $\boldsymbol{\Phi}$ through the POD operation [28, 45], by extracting the eigenvectors of the covariance matrix $\mathbf{C} = \mathbf{U}^T \cdot \mathbf{U}$, through singular value decomposition. We then perform a truncation to reduce the basis vectors $\boldsymbol{\Phi}$ and formulate a lower rank version $\hat{\boldsymbol{\Phi}}$ by preserving the first k ($k \ll S$) columns of $\boldsymbol{\Phi}$ that correspond to the largest eigenvalues. Consequently, a new amplitude matrix $\hat{\mathbf{A}}$ writes:

$$\hat{\mathbf{A}} = \hat{\boldsymbol{\Phi}}^T \cdot \mathbf{U}. \quad (12)$$

Note here that one can recover the original data using the reduced model by the following approximation.

$$\mathbf{U} \approx \hat{\Phi} \cdot \hat{\mathbf{A}}. \quad (13)$$

At this step, we link the structural response data to the crack parameters through Radial Basis Function (RBF) and a coefficient matrix \mathbf{B} and an interpolation matrix \mathbf{G} as $\mathbf{B} \cdot \mathbf{G} = \hat{\mathbf{A}}$.

In the case where \mathbf{G} is a non-singular matrix, one can write the following expression

$$\mathbf{B} = \hat{\mathbf{A}} \cdot \mathbf{G}^{-1}. \quad (14)$$

Here, the matrix of interpolation \mathbf{G} is persymmetric, and it englobes the RBF function: $\mathbf{g}_i(\mathbf{p}) = |\mathbf{p} - \mathbf{p}_i|$ as such

$$\mathbf{G} = \begin{bmatrix} g(|\mathbf{p}_1 - \mathbf{p}_1|) & g(|\mathbf{p}_1 - \mathbf{p}_2|) & \dots & g(|\mathbf{p}_1 - \mathbf{p}_N|) \\ g(|\mathbf{p}_2 - \mathbf{p}_1|) & g(|\mathbf{p}_2 - \mathbf{p}_2|) & \dots & g(|\mathbf{p}_2 - \mathbf{p}_N|) \\ \vdots & \vdots & \ddots & \vdots \\ g(|\mathbf{p}_N - \mathbf{p}_1|) & g(|\mathbf{p}_N - \mathbf{p}_2|) & \dots & g(|\mathbf{p}_N - \mathbf{p}_N|) \end{bmatrix} \quad (15)$$

$\mathbf{g}_i(\mathbf{p})$ calculated for each parameter in the matrix \mathbf{G} where \mathbf{p}_i is the parameter corresponding to \mathbf{U}_i ($i=1,2,\dots,N$). The argument of the i -th RBF is the distance $|\mathbf{p} - \mathbf{p}_i|$, \mathbf{p} and \mathbf{p}_i being respectively current and reference parameters.

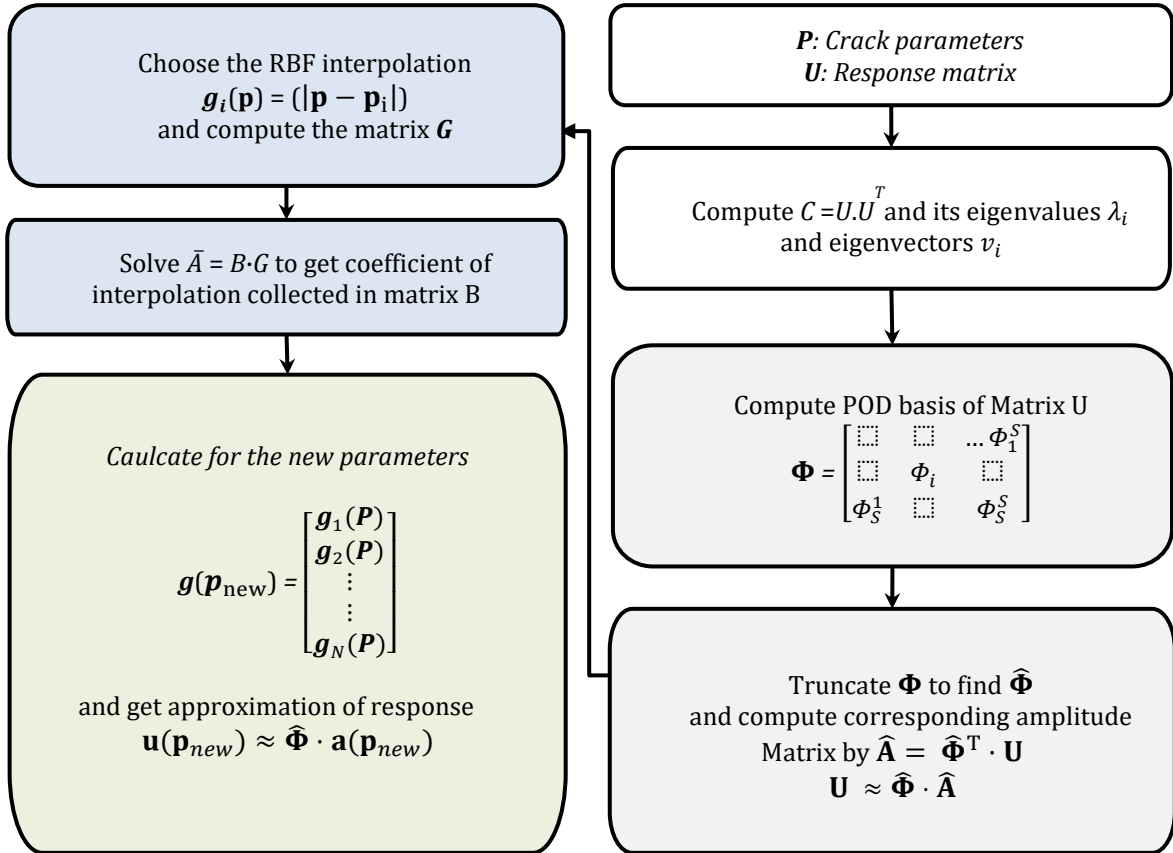


Figure 5. POD-RBF methodology

After we calculate the coefficient matrix \mathbf{B} , a low-dimensional model of Eq. (14) is put in vector form, as follows, and used to calculate the amplitude vector $\mathbf{a}(\mathbf{p}_{new})$ for new parameters, outside the positions of the sensors:

$$\mathbf{a}(\mathbf{p}_{new}) = \mathbf{B} \cdot \mathbf{g}(\mathbf{p}_{new}) \quad (15)$$

Eq. (14) rewrites then in a vector form to calculate the interpolated data \mathbf{u} corresponding to the new cracks parameter \mathbf{p}_{new} . This way, we calculate the structural response corresponding to the new crack:

$$\mathbf{u}(\mathbf{p}_{new}) \approx \hat{\Phi} \cdot \mathbf{a}(\mathbf{p}_{new}) \quad (16)$$

The POD-RBF model, Eq 16. is, therefore, able to reproduce unknown structural responses corresponding to any set of crack parameters \mathbf{p} . However, note that it can lead to weak precision due to the extrapolation outside the range of measured crack parameters \mathbf{p} . Fig.5. summarize building the POD-RBF.

4 Identification using static boundary displacement

4.1 FEM simulation setup

For this two-dimensional stress analysis problems under plane strain conditions, eight basic independent parameters: $\mathbf{u}, \mathbf{v}, \boldsymbol{\varepsilon}_x, \boldsymbol{\varepsilon}_y, \boldsymbol{\gamma}_{xy}, \boldsymbol{\sigma}_x, \boldsymbol{\sigma}_y, \boldsymbol{\tau}_{xy}$ [46]. u and v are the displacements in X and Y direction respectively, $\boldsymbol{\varepsilon}_x, \boldsymbol{\varepsilon}_y$ are normal strain components, $\boldsymbol{\gamma}_{xy}$ is the Shear strain component, $\boldsymbol{\sigma}_x, \boldsymbol{\sigma}_y$ are normal stress components and $\boldsymbol{\tau}_{xy}$ is the shear stress component.

Elastostatics here means the study of linear elasticity under the conditions of equilibrium, in which all forces on the elastic body sum to zero and $\boldsymbol{\tau}_{xy} = \boldsymbol{\tau}_{yx}$. The displacements are not a function of time. Furthermore, the components of Cauchy's strain tensor for minor strain problems follow this strain displacement relationship:

$$\boldsymbol{\varepsilon}_x = \frac{\partial \mathbf{u}}{\partial x}, \quad \boldsymbol{\varepsilon}_y = \frac{\partial \mathbf{v}}{\partial y}, \quad \boldsymbol{\gamma}_{xy} = \frac{\partial \mathbf{v}}{\partial x} + \frac{\partial \mathbf{u}}{\partial y} \quad (16)$$

For isotropically elastic materials, the stress components are related to the strain components by Hooke's law as $\boldsymbol{\sigma} = \mathbf{E}\boldsymbol{\varepsilon}$ where \mathbf{E} is Young's modulus.

For the FEM simulation, we consider a plate with 1mm thickness, 30 mm height, and 10 mm width (Fig. 6). With a Young modulus \mathbf{E} of 210 GPa and Poisson coefficient of 0.3. Under a displacement of 0.3 mm at the upper and lower sides of the plate.

The vertical side is meshed using 120 quadrilaterals and the horizontal side with 40 elements. The meshing of the crack consists of two types of areas: the crack tips, covering both crack endings, and the middle of the crack. Crack tips are meshed by the sweep function. The circular area has 0.5 mm of the radius, divided into 20 elements along the contour of the circle. And 10 elements along the radius of the circle. There is a total of 200 elements concentrated at each tip of the crack.

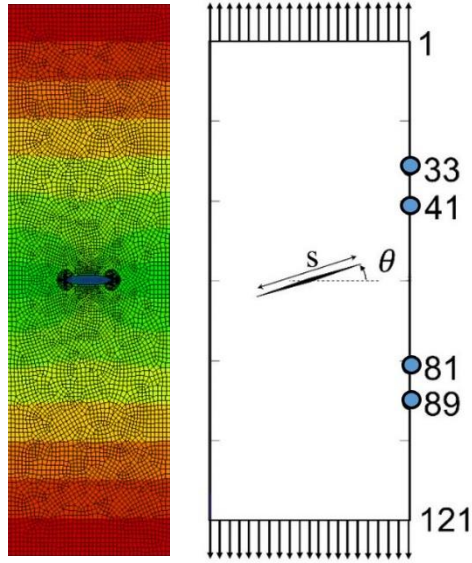


Figure 6. Cracked specimen

4.2. The POD-RBF model validation

The snapshot matrix \mathbf{U} consists of the measured displacement at the right vertical side (Eq. 10). The crack length s and the crack orientation θ are the parameters that are subject to identification within this interval:

$$0 \text{ mm} \leq s \leq 5 \text{ mm} \text{ and } 0^\circ \leq \theta \leq 60^\circ . \quad (18)$$

The reduced model is constructed using the boundary displacement measured from 111 FE simulations, with length and orientation values of crack obtained by dividing the intervals of (Eq. 18) into steps of 6° for θ and 0.5 mm for s . Plus, one case representing structure without crack.

We truncate the reduced basis model using the first 16 vectors, at the point where the ratio between the eigenvalues of the neglected vectors and the retained ones becomes less than 10^{-11} , as shown in Fig.7. Fig. 8 compares the POD-RBF predictions with the FE boundary displacements.

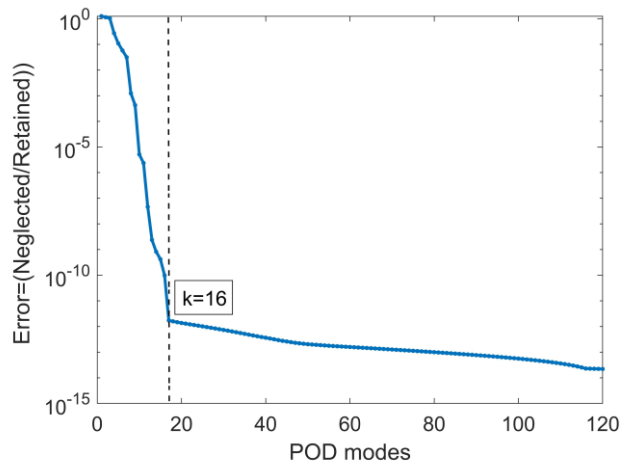


Figure 7. The truncation point on the Elastostatic model

Fig. 6 report the error between both boundary displacements in each boundary node. For a crack with a length of 3.3 mm and with an orientation of 37.5° . This figure highlights a good agreement between the model predictions and FE results, except around the middle of the plate, around node 62, where appears a sudden divergence. We see this discrepancy because the node 62 at the center line, where displacements are close to zero independently from the loading level. This effect makes the error values that can be considered small appear very large in extremely small-displacement values.

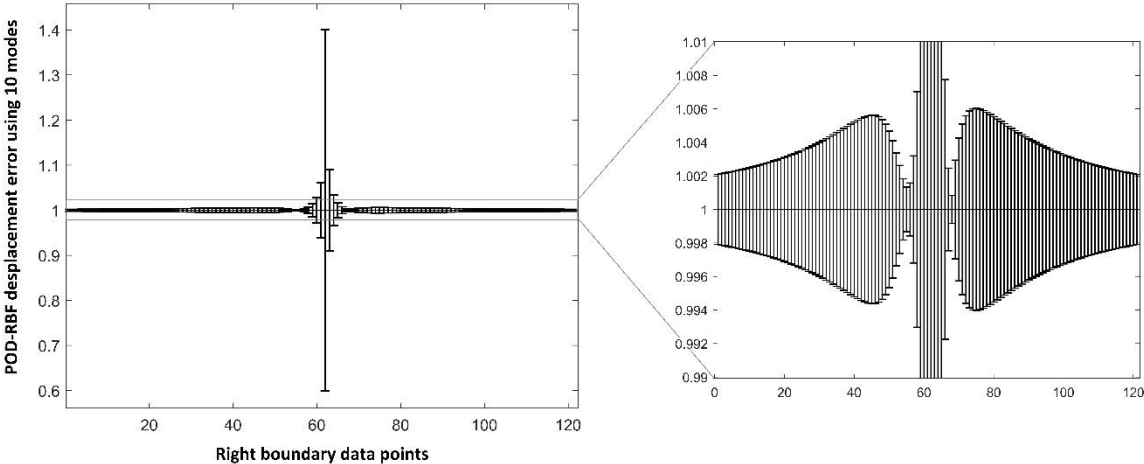


Figure 8. The error of POD-RBF boundary displacement

4.3. Fitness evaluation based on all boundary data

10 test cracks are studied (C1 to C10) with different sizes and orientations. To solve this inverse problem, YA is run 20 times for each test crack, using a population of 30, and the maximum number of iterations is 100. Table 1 present the results in the form of an average over the 20 runs.

Figs. 9 displays the example of fitness convergence and the convergence of the crack parameters for the cases C2 (Table 1). In Fig. 9(a) at the 40th iteration, the function $f(P)$ Reach a value of $\sim 1.0^{-4}$. While Fig. 9 (b) highlights that the predicted crack length converged toward a solution near the exact value after the 40th iteration. However, the crack orientation in Fig.9 (c) converged toward a solution close to the exact value after the 70th iteration.

The test cracks cover the different sizes and orientations, with cases of the same size and variable orientations. Also, cases with the same orientations and variable size. The results in table 1. present error as the absolute difference between the actual and predicted crack. The maximum error for crack size is 0.61 mm in the case of the largest crack. As well as for crack orientation is 3.94° also in the case of largest orientation.

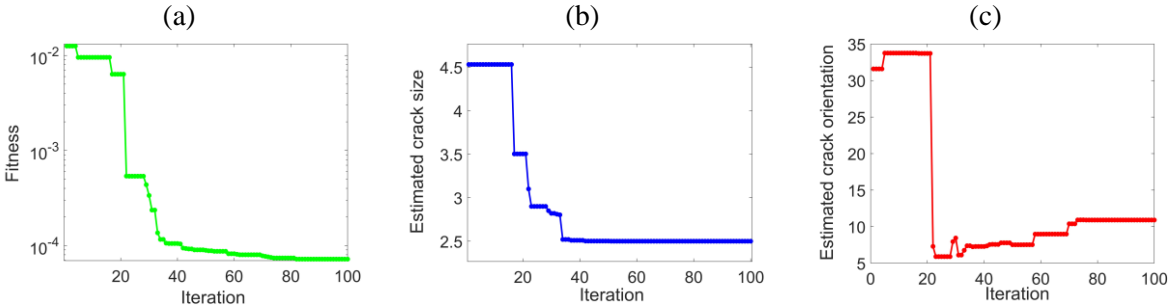


Figure 9. C2 Crack identification

Table 1. Identified cracks using boundary displacement at all boundary nodes

Studied cases	Real crack		Estimated crack		Error	
	s (mm)	θ ($^{\circ}$)	s (mm)	θ ($^{\circ}$)	s (%)	θ (%)
C1	1.2	10.0	1.33	10.18	10.83	1.8
C2	2.5	10.0	2.06	10.06	17.6	0.6
C3	3.3	10.0	3.57	9.43	8.18	5.7
C4	4.9	10.0	4.97	10.35	1.42	3.5
C5	1.2	15.0	1.32	14.22	10	5.2
C6	1.2	37.5	1.34	35.29	11.6	5.89
C7	3.3	17.0	3.51	14.27	6.36	16.05
C8	3.3	37.5	3.19	37.49	3.33	0.02
C9	3.3	60.0	3.12	56.06	5.45	6.56
C10	5.0	37.5	4.39	33.88	12.2	9.65

4.4 Fitness evaluation based on noisy data

We study the sensitivity of the crack identification approach against measurement uncertainty. We simulate it by introducing white Gaussian noise to the input displacement vector. Four levels of 1%, 2%, 3%, 5%, and 10%.

Fig. 10 present the average errors across all crack cases as a function of the noise level. The error here is the absolute difference between the actual crack parameter and the predicted ones. This figure shows that errors increase with the rise of the noise levels. However, one can note that the effect on crack orientation prediction is more significant, reaches 40% for the highest noise level of 10%. These results suggest that the approach proposed in this work shows higher stability for crack size prediction than crack orientation. However, the 5% and 10% noises are far more extensive than measurement uncertainty tolerance levels in the industry.

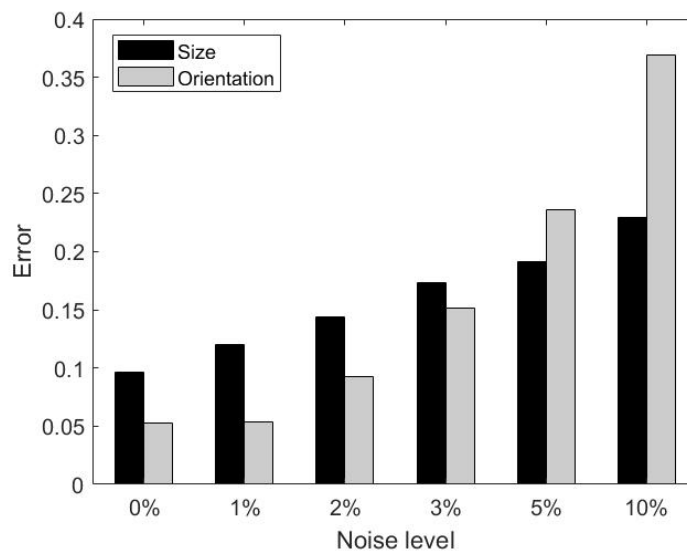


Figure 10. Effect of noise level on the average prediction error for all cracks

In reasonable uncertainty levels of 1% and 2%, the results slightly increase the crack size and orientation error. It is noticeable that the orientation errors exceed size errors beyond 3% noise. This is because variation in crack orientation reflects on the displacement at a smaller number of boundary nodes than the variation in crack length. Therefore, it is harder to distinguish between boundary displacements corresponding to different crack orientations from the inverse problem perspective.

4.5 Identification using a small number of sensor points

The results discussed above were determined using the displacements of all boundary nodes of the specimen. This section discusses the results obtained using only four sensor points represented in Fig. 6 by circles. The nodes 33, 41, 81, and 89 are located at 22 mm, 20 mm, 10 mm, and 8 mm. Under a noise level of 2%. Table 2. present the results. They showed that reducing the sensor point number to 4 did not globally affect the identification performance of the model.

Table 2. Identified cracks using boundary displacement at four nodes

Studied cases	Real crack		Estimated crack		Error	
	s (mm)	θ ($^{\circ}$)	s (mm)	θ ($^{\circ}$)	s (%)	θ (%)
C1	1.2	10	1.51	9.74	25.83	2.6
C2	2.5	10	2.99	9.06	19.6	9.4
C3	3.3	10	3.51	10.88	6.36	8.8
C4	4.9	10	4.94	10.15	0.81	1.5
C5	1.2	15	1.49	14.85	24.16	1
C6	1.2	37.5	1.30	36.94	8.33	1.49
C7	3.3	17	3.44	18.04	4.24	6.11
C8	3.3	37.5	3.11	38.06	5.75	1.49
C9	3.3	60	3.16	58.48	4.242	2.53
C10	5	37.5	4.52	36.06	9.6	3.84

4.6 Optimization algorithms performances

In iterative identification problems, the computational time is an issue because of the repetitive nature of the computation. Fitness evaluation is the most significant contributor to computational cost. However, since the evaluation time is considered invariable for the same problem, the optimization convergence speed becomes an important issue. Therefore, the efficiency of the identification calculation highly depends on the chosen optimization algorithm.

CS is a well-known search algorithm inspired by the parasitic reproduction strategy of cuckoo birds. They lay their eggs in the nests of the host's birds, who may discover that and either destroy the egg or abandon the nest [42]; in the formulation of this algorithm, the number of available host nests is constant. Thus, a host can discover an alien egg with a probability of P_a between 0 and 1.

The TLBO is a parameter-less algorithm that mimics teaching and learning abilities in a classroom [43], with two primary stages in each iteration. The teacher phase, where the best solution influences all population members. And on the other hand, there is the learning phase. Here the fitnesses of individuals are compared with each other. GWO is a widely used optimization algorithm inspired by the hunting behavior of a grey wolf pack, and it simulates the hierarchical system by ranking by fitness values.

In this case, we consider YA, GWO, and TLBO along with CS using the data issued from the four sensor points described earlier, with a 2% noise level. For the sake of performance comparison, each algorithm performs 20 runs, with a population size of 30 and a maximum number of iterations equal to 100. For CS, the probability P_a is chosen equal to 0.25. Fig.10 depicts the average fitness convergence for these algorithms in the case of crack C8 ($S=3.3$ mm, $\theta =37.5^\circ$). And Table 3 report the analysis of the results.

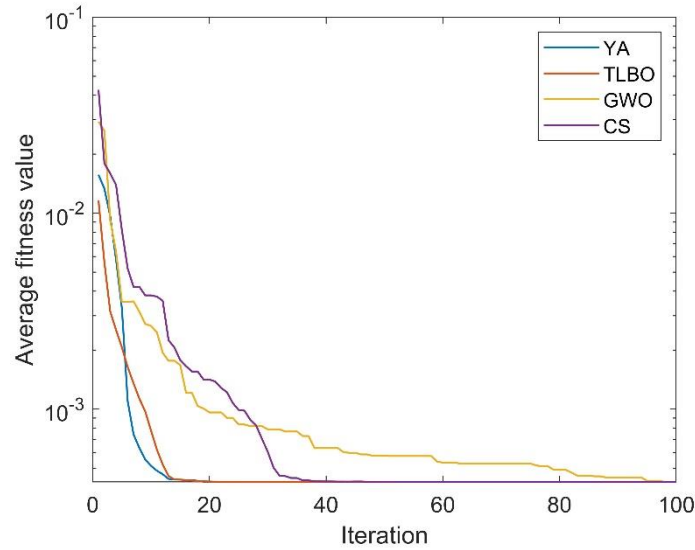


Figure 11. Average fitness convergence by YA, TLBO, GWO, and CS algorithms in C8

Fig. 11 shows that although all algorithms converge to the same fitness value, YA and TLBO algorithms converge rapidly, around the 20th iteration, relatively to CS and GWO that converge before the 40 and 80 iterations, respectively.

We note that in terms of identification quality, the results show that the crack size and orientation can be estimated precisely by all algorithms, despite the noise in the data issued and the low number of sensors. However, YA and TLBO algorithms provided quick convergence to the optimum, which means fewer iterations can be sufficient. Furthermore, YA and GWO algorithms are advantageous in computational time because both these algorithms are based on very few steps and require a single evaluation in each iteration.

Table 3. Performance of YA, TLBO, GWO, and CS algorithms in case C8 using four sensor points under 2% noise.

	Average Time (s)	Best fitness value	The standard deviation of the fitness	Best crack size mm (error %)	Best crack orientation° (error %)
YA	15.54	$4.251 \cdot 10^{-4}$	$1.34 \cdot 10^{-17}$	3.10 (6.06)	37.40 (0.26)
TLBO	31.72	$4.251 \cdot 10^{-4}$	$2.81 \cdot 10^{-17}$	3.10 (6.06)	37.40 (0.26)
GWO	15.63	$4.254 \cdot 10^{-4}$	$1.01 \cdot 10^{-8}$	3.10 (6.06)	37.06 (1.17)
CS	30.23	$4.252 \cdot 10^{-4}$	$4.87 \cdot 10^{-7}$	3.10 (6.06)	37.62 (0.32)

5 Identification using dynamic analysis

5.1. Experimental setup

This section expands on the study made in Ref [41] using experimental data issues from a frequency response of a 400mm by 330 mm metallic plate, shown in Fig. 12. Young's modulus, 2.25 10¹¹ (N/M²), the Poisson's ratio 0.3, the density of 7850 kg/m³, and the thickness of 2 mm.

6 PCB Accelerometers (356A15), excited with a PCB hammer (086C03) to measure the vibration. Fig.12 shows the positions of the six accelerometers. Fig.13 shows the experimental setup.

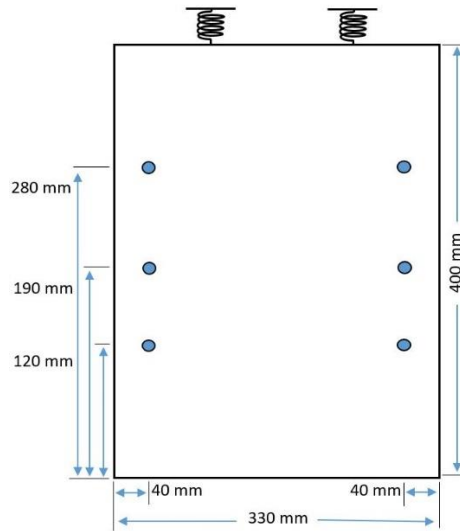


Figure 12. Plate dimensions and accelerometer positions



Figure 13. Experimental setup.

5.2. POD-RBF based on experimental data

We consider in this study three crack orientations. The horizontal crack (0°) and the crack at an angle of 45° start from the center of the left side. On the other hand, the vertical crack (90°) starts from the center of the top side of the plate. In this study, the vibrational response is considered for crack varying between 0 (no crack) and 80 mm. with a step of 10 mm.

Using the Frequency Response Function (FRF) measured for 27 cracks, a POD-RBF model is constructed and truncated with 19 vectors. In this point, the ratio between the neglected eigenvalues and the retained ones is less than 10^{-10} . As shown in Fig. 14. Fig. 15 shows the experimental FRF at crack length 25 mm and orientation of 45° , compared to the predicted FRF calculated by the POD-RBF model. This figure highlights a good agreement between the model predictions and experimental measurement at modes positions.

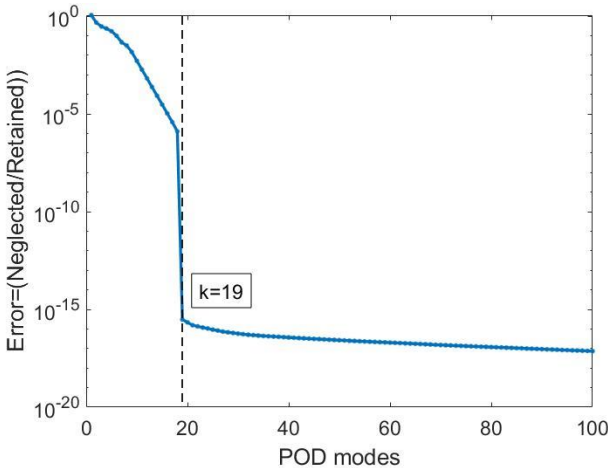


Figure 14. The truncation point on the dynamic model

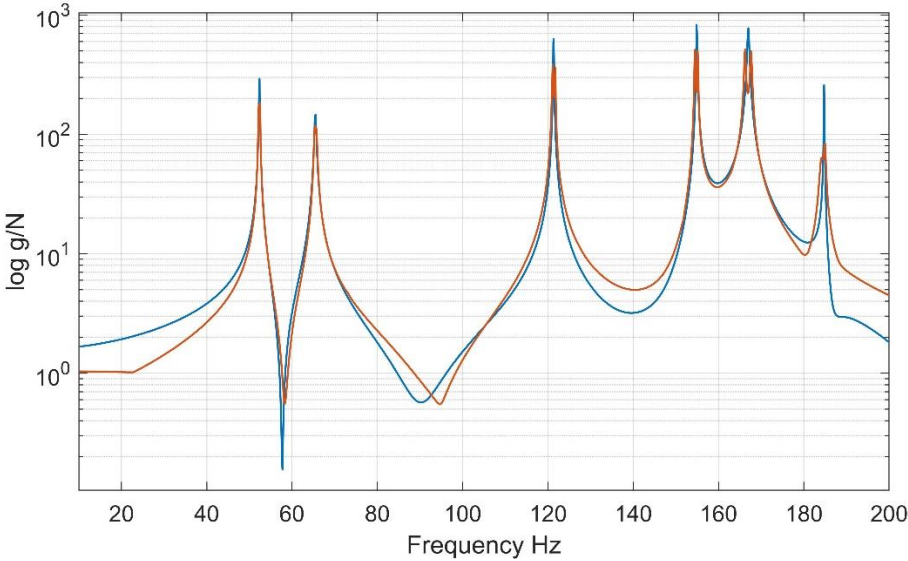


Figure 15. Experimental FRF from 25 mm crack at 45° vs. predicted using POD-RBF

5.3. Fitness evaluation base on experimental data

We consider in this study seven crack cases. To solve this inverse problem, the YA is run 20 times for each test crack to minimize Eq. 9. using a population of 30, the maximum number of iterations is 100. Table 4 summarizes the results in the form of an average over the 20 runs.

Table 4 presented the error as the absolute difference between the actual and predicted crack. The results show that the maximum error for size prediction is 2.76 mm, and the orientation is 0.43° .

Table 4. Identified cracks based on the experimental dynamic study

Studied cases	Real crack		Estimated crack		Error	
	s (mm)	θ ($^\circ$)	s (mm)	θ ($^\circ$)	s (%)	θ (%)
C11	25	0	22.24	0.032	11.04	-
C12	75	0	73.29	$1.26 \cdot 10^{-5}$	2.28	-
C13	25	45	24.89	45.05	0.44	0.11
C14	75	45	74.73	44.57	0.36	0.95
C15	10	90	7.710	89.99	22.9	0.01
C16	50	90	49.82	89.99	0.36	0.01
C17	75	90	74.05	89.94	1.26	0.06

An example of fitness convergence and the convergence of the crack parameters is presented in Fig 16 for cases C14 (Table 4). In Fig. 16(a), The fitness value $f(P)$ Reach a value of $1.0 \cdot 10^{-3}$ before the 20th iteration. For example, fig. 16(b) and Fig.17 (c) show that crack size and orientation converged to a solution close to the exact value in 20 iterations.

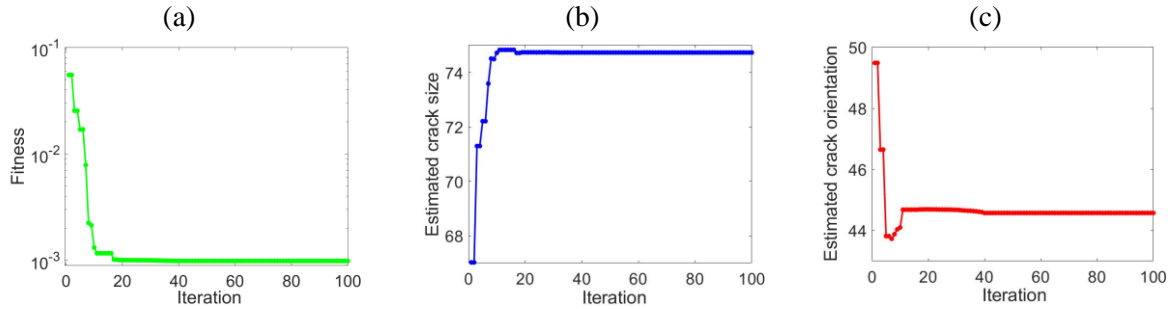


Figure 16. C14 crack parameter identification versus iterations

5.4. Optimization algorithms performances

We compare the performance of the four algorithms YA, GWO, TLBO, and CS in this section. Each algorithm performs 20 runs, where the population size is 30, and the maximum number of iterations is 100. Fig. 17 depicts the average fitness convergence for these algorithms in the case of crack C14 ($S=75$ mm, $\theta =45^\circ$). And Table 5 report the analysis of the results. Table 6, on the other hand, report the performances of the algorithms in the case C11, where the error is high.

Fig. 17 shows that although all algorithms converge to the same fitness value, YA and TLBO algorithms converge rapidly, around the 30th iteration, relatively to CS that converge before the 50th and GWO converged at 100 iterations.

The results show that the crack size and its orientation can be estimated precisely by all algorithms in terms of identification quality. However, YA and TLBO algorithms provided quick convergence, with an advantage over TLBO. Finally, we should mention that TLBO uses twice the number of evaluations in each iteration as opposed to the other algorithms. Thus it spends double the computational cost on evaluation. This observation is apparent in table 5 results. Results in Table 6 suggest that the high error found earlier in table 4 is due to the limitation of the POD-RBF model. As the model is built

using a limited set of experimental results, POD-RBF estimation accuracy is lower when cases near the boundaries of the known data, like in the case of C11 and the case C15, that correspond to 0° and 90° respectively.

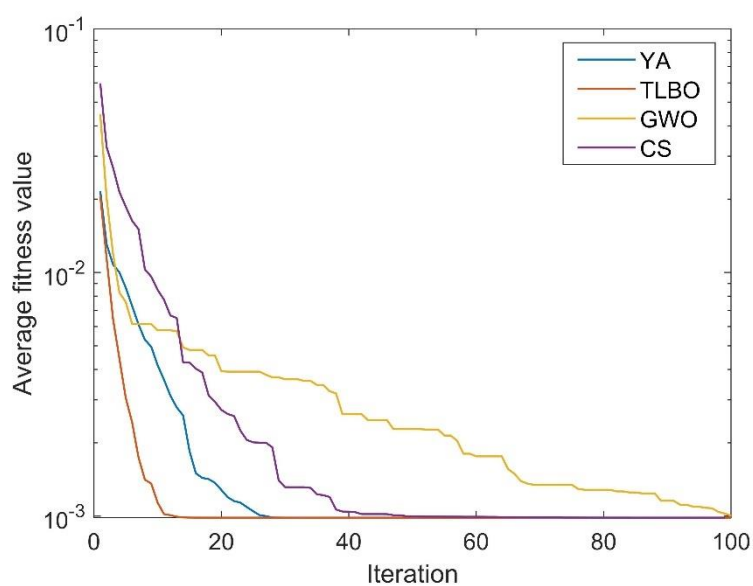


Figure 17. Average fitness convergence by YA, TLBO, GWO, and CS algorithms in C14

Table 5. Performance of YA, TLBO, GWO, and CS algorithms in case C14

	Average Time (s)	Best fitness value	The standard deviation of the fitness	Best crack size mm (error %)	Best crack orientation ^o (error %)
YA	12.30	0.000985	$2.4 \cdot 10^{-15}$	74.73 (0.36)	44.57 (0.95)
TLBO	24.11	0.000985	$8.44 \cdot 10^{-15}$	74.73 (0.36)	44.53 (0.95)
GWO	12.72	0.001015	$2.93 \cdot 10^{-5}$	74.72 (0.37)	44.57 (1.04)
CS	23.96	0.000985	$1.68 \cdot 10^{-8}$	74.73 (0.36)	44.57 (0.95)

Table 6. Performance of YA, TLBO, GWO, and CS algorithms in case C11

	Average Time (s)	Best fitness value	The standard deviation of the fitness	Best crack size mm (error %)	Best crack orientation ^o
YA	12.35	1.63 E-03	$6.51 \cdot 10^{-7}$	22.24 (11.04)	0.03
TLBO	25.33	1.63 E-03	$3.21 \cdot 10^{-17}$	22.17 (11.32)	0.00
GWO	12.49	1.63 E-03	$4.56 \cdot 10^{-10}$	22.18 (11.28)	0.00
CS	24.68	1.63 E-03	$2.79 \cdot 10^{-9}$	22.17 (11.32)	0.00

6 Conclusion

We have presented in this paper a new metaheuristic algorithm and applied it to the study of inverse crack identification based on the POD-RBF technique. We considered two studies, namely, Elastostatic based on FEM analysis and a vibrational study based on experimental data. The method is effective compared to recently published algorithms, such as GWO, CS, and TLBO.

Moreover, we have shown that the presented method is stable concerning noisy input data, mimicking the measurement uncertainty, and limited sensors.

We compare the performance of the suggested algorithm to GWO, CS, and TLBO algorithms. The results indicate that these algorithms can efficiently identify the size and orientation of the crack accurately, with YA having an advantage in terms of computation time.

The future study combines the new algorithm YA with the local optimization method in crack detections using eddy current tomography. As well as investigate the performance of metaheuristic algorithms for robust minimization procedures based on DNN, as such methods provide higher flexibility in optimization and uncertainty evaluation and constitute frameworks to solve both inverse and forward problems.

Replication of Results

The results presented in this article can replicate by implementing the data structures and algorithms presented in the article. All the references are reported in the paper, as well as the algorithm. In any case, the code (developed in MATLAB) is available upon request from the authors; the YUKI algorithm package is planned to be released after the acceptance of this paper.

References

1. Friswell, M.I., *Damage identification using inverse methods*. Philosophical Transactions of the Royal Society A: Mathematical, Physical and Engineering Sciences, 2007. **365**(1851): p. 393-410.
2. Bui, H.D., *Fracture mechanics: inverse problems and solutions*. Vol. 139. 2007: Springer Science & Business Media.
3. Stavroulakis, G.E., *Inverse and crack identification problems in engineering mechanics*. Vol. 46. 2013: Springer Science & Business Media.
4. Mellings, S. and M. Aliabadi, *Flaw identification using the boundary element method*. International journal for numerical methods in engineering, 1995. **38**(3): p. 399-419.
5. Du, C., et al., *Dynamic XFEM-based detection of multiple flaws using an improved artificial bee colony algorithm*. Computer Methods in Applied Mechanics and Engineering, 2020. **365**: p. 112995.
6. Rabinovich, D., D. Givoli, and S. Vigdergauz, *Crack identification by 'arrival time' using XFEM and a genetic algorithm*. International Journal for Numerical Methods in Engineering, 2009. **77**(3): p. 337-359.
7. Haddar, H., Z. Jiang, and M.K. Riahi, *A robust inversion method for quantitative 3D shape reconstruction from coaxial eddy current measurements*. Journal of Scientific Computing, 2017. **70**(1): p. 29-59.
8. Haddar, H. and M. Riahi, *Near-Field Linear Sampling Method for Axisymmetric Eddy Current Tomography*. arXiv preprint arXiv:2103.01207, 2021.
9. Nanthakumar, S., et al., *Detection of material interfaces using a regularized level set method in piezoelectric structures*. Inverse Problems in Science and Engineering, 2016. **24**(1): p. 153-176.
10. Alessandri, C. and V. Mallardo, *Crack identification in two-dimensional unilateral contact mechanics with the boundary element method*. Computational mechanics, 1999. **24**(2): p. 100-109.
11. Amoura, N., et al., *Axisymmetric and two-dimensional crack identification using boundary elements and coupled quasi-random downhill simplex algorithms*. Engineering Analysis with Boundary Elements, 2010. **34**(6): p. 611-618.
12. Vossou, C.G., I.N. Koukoulis, and C.G. Provatidis, *Genetic Combined with a Simplex Algorithm as an Efficient Method for the Detection of a Depressed Ellipsoidal Flaw using the Boundary Element Method*. International Journal of Applied Mathematics and Computer Sciences, 2007. **4**(2).
13. Burczynski, T. and W. Beluch, *The identification of cracks using boundary elements and evolutionary algorithms*. Engineering Analysis with Boundary Elements, 2001. **25**(4): p. 313-322.
14. Hattori, G. and A. Sáez, *Damage identification in multifield materials using neural networks*. Inverse Problems in Science and Engineering, 2013. **21**(6): p. 929-944.

15. Khatir, S. and M.A. Wahab, *Fast simulations for solving fracture mechanics inverse problems using POD-RBF XIGA and Jaya algorithm*. Engineering Fracture Mechanics, 2019. **205**: p. 285-300.
16. Samir, K., et al. *Genetic algorithm based objective functions comparative study for damage detection and localization in beam structures*. in *Journal of Physics: Conference Series*. 2015. IOP Publishing.
17. Nanthakumar, S., T. Lahmer, and T. Rabczuk, *Detection of multiple flaws in piezoelectric structures using XFEM and level sets*. Computer Methods in applied Mechanics and engineering, 2014. **275**: p. 98-112.
18. Nguyen-Tuan, L., S.S. Nanthakumar, and T. Lahmer, *Identification of multiple flaws in dams using inverse analysis based on hydro-mechanical XFEM and level sets*. Computers and Geotechnics, 2019. **110**: p. 211-221.
19. Alalade, M., et al., *Damage identification in gravity dams using dynamic coupled hydro-mechanical XFEM*. International Journal of Mechanics and Materials in Design, 2018. **14**(1): p. 157-175.
20. Chatterjee, A., *An introduction to the proper orthogonal decomposition*. Current science, 2000. **78**(7): p. 808-817.
21. Benaissa, B., et al. *Application of proper orthogonal decomposition and radial basis functions for crack size estimation using particle swarm optimization*. in *Journal of Physics: Conference Series*. 2017. IOP Publishing.
22. Samir, K., et al., *Damage detection in CFRP composite beams based on vibration analysis using proper orthogonal decomposition method with radial basis functions and cuckoo search algorithm*. Composite Structures, 2018. **187**: p. 344-353.
23. Winton, C., et al., *Application of Proper Orthogonal Decomposition (POD) to inverse problems in saturated groundwater flow*. Advances in Water Resources, 2011. **34**(12): p. 1519-1526.
24. Ostrowski, Z., R. Bialecki, and A. Kassab, *Solving inverse heat conduction problems using trained POD-RBF network inverse method*. Inverse Problems in Science and Engineering, 2008. **16**(1): p. 39-54.
25. Brigham, J.C. and W. Aquino, *Inverse viscoelastic material characterization using POD reduced-order modeling in acoustic-structure interaction*. Computer Methods in Applied Mechanics and Engineering, 2009. **198**(9): p. 893-903.
26. Rogers, C.A., et al., *An inverse POD-RBF network approach to parameter estimation in mechanics*. Inverse Problems in Science and Engineering, 2012. **20**(5): p. 749-767.
27. Wang, S., S. Khatir, and M.A. Wahab, *Proper Orthogonal Decomposition for the prediction of fretting wear characteristics*. Tribology International, 2020. **152**: p. 106545.
28. Buljak, V. and G. Maier, *Proper orthogonal decomposition and radial basis functions in material characterization based on instrumented indentation*. Engineering Structures, 2011. **33**(2): p. 492-501.
29. Hoang, K., et al., *Rapid identification of material properties of the interface tissue in dental implant systems using reduced basis method*. Inverse Problems in Science and Engineering, 2013. **21**(8): p. 1310-1334.
30. Broomhead, D.S. and D. Lowe, *Radial basis functions, multi-variable functional interpolation and adaptive networks*. 1988, DTIC Document.
31. Levasseur, S., et al., *Statistical inverse analysis based on genetic algorithm and principal component analysis: method and developments using synthetic data*. International journal for numerical and analytical methods in geomechanics, 2009. **33**(12): p. 1485-1511.
32. Bolzon, G. and V. Buljak, *An indentation - based technique to determine in - depth residual stress profiles induced by surface treatment of metal components*. Fatigue & Fracture of Engineering Materials & Structures, 2011. **34**(2): p. 97-107.
33. Bolzon, G., et al., *Assessment of elastic-plastic material parameters comparatively by three procedures based on indentation test and inverse analysis*. Inverse Problems in Science and Engineering, 2011. **19**(6): p. 815-837.
34. Buljak, V., *Inverse Analyses with Model Reduction: Proper Orthogonal Decomposition in Structural Mechanics*. 2012: Springer.
35. Bolzon, G. and V. Buljak, *An effective computational tool for parametric studies and identification problems in materials mechanics*. Computational mechanics, 2011. **48**(6): p. 675-687.
36. Druault, P., P. Guibert, and F. Alizon, *Use of proper orthogonal decomposition for time interpolation from PIV data*. Experiments in fluids, 2005. **39**(6): p. 1009-1023.
37. Bocciairelli, M., et al., *An inverse analysis approach based on a POD direct model for the mechanical characterization of metallic materials*. Computational Materials Science, 2014. **95**: p. 302-308.
38. Anitescu, C., et al., *Artificial neural network methods for the solution of second order boundary value problems*. Computers, Materials and Continua, 2019. **59**(1): p. 345-359.
39. Rabinovich, D., D. Givoli, and S. Vigdergauz, *XFEM - based crack detection scheme using a genetic algorithm*. International Journal for Numerical Methods in Engineering, 2007. **71**(9): p. 1051-1080.

40. Benaissa, B., et al., *Crack identification using model reduction based on proper orthogonal decomposition coupled with radial basis functions*. Structural and Multidisciplinary Optimization, 2016. **54**(2): p. 265-274.
41. Khafir, S., et al., *Improved ANN technique combined with Jaya algorithm for crack identification in plates using XIGA and experimental analysis*. Theoretical and Applied Fracture Mechanics, 2020. **107**: p. 102554.
42. Yang, X.-S. and S. Deb, *Engineering optimisation by cuckoo search*. International Journal of Mathematical Modelling and Numerical Optimisation, 2010. **1**(4): p. 330-343.
43. Rao, R. and V. Patel, *An elitist teaching-learning-based optimization algorithm for solving complex constrained optimization problems*. International Journal of Industrial Engineering Computations, 2012. **3**(4): p. 535-560.
44. Mirjalili, S., S.M. Mirjalili, and A. Lewis, *Grey wolf optimizer*. Advances in engineering software, 2014. **69**: p. 46-61.
45. Benaissa, B., et al., *Crack identification using model reduction based on proper orthogonal decomposition coupled with radial basis functions*. Structural and Multidisciplinary Optimization, 2016: p. 1-10.
46. Bonnet, M. and A. Constantinescu, *Inverse problems in elasticity*. Inverse problems, 2005. **21**(2): p. R1.